Journal of Computational Physics **168,** 316–338 (2001)
doi:10.1006/jcph.2001.6698, available online at http://www.idealibrary.com on IDEAL®

An Accurate ENO Driven Multigrid Method Applied to 3D Turbulent Transonic Flows[1,2]

B. Epstein,* A. Averbuch,† and I. Yavneh‡

*Computer Science Department, The Academic College of Tel-Aviv-Yaffo, 4 Antokolsky Street, Tel Aviv 64044, Israel; †School of Mathematical Sciences, Tel Aviv University, Tel Aviv 69978, Israel; and ‡Faculty of Computer Science, Technion, Haifa 32000, Israel
E-mail: amir@math.tau.ac.il

Received November 16, 1999; revised April 20, 2000

A multigrid method for computing steady solutions of the compressible Navier–Stokes equations is described. The convection part of the equations is approximated by a simple low-order upwind-biased scheme employed for multigrid relaxation in combination with a higher order essentially non-oscillatory (ENO) scheme used to supply a *defect correction* to the right-hand side of the discrete equations on the locally finest multigrid levels in a way ensuring the overall high accuracy of the solution. A damping technique is employed to stabilize and accelerate the defect-correction process. © 2001 Academic Press

Key Words: Navier–Stokes; ENO; multigrid; defect correction; turbulent flows.

1. INTRODUCTION

This work is motivated by the necessity to improve the ability of Navier–Stokes solvers to predict correctly major aerodynamic characteristics of flow (such as drag coefficient) in a turbulent transonic regime. In this regime linearly stable high-order methods are often unstable and most standard methods add artificial dissipation (explicitly or implicitly as in TVD schemes) in order to ensure the nonlinear stability. This leads to a loss of accuracy as the details of flow near the shock (damped by artificial viscosity) may considerably affect large-scale properties of the flow [1, 2]. Therefore, numerical results frequently lack sufficient credibility from the viewpoint of practical aerodynamics.

ENO schemes, introduced by Harten *et al.* [3] and further simplified by Shu and Osher [4], use the idea of an adaptive stencil interpolation from the regions where the solution is

[1] Partial results of this paper were presented in the 14th AIAA CFD Conference, pp. 705–715, Norfolk, Virginia, June 1999.

[2] This research was supported by Israeli Ministry of Science and Technology in the years 1997–1999.

0021-9991/01 $35.00

smoother, and thus achieve accuracy of a uniformly high order. In previous publications [5–7] a finite-volume numerical method based on the ENO approach was introduced and applied to realistic aerodynamic geometries. Accurate results were achieved on relatively coarse grids without the need for any additional dissipation. The method was verified for a variety of inviscid and viscous flows in different flow regimes including turbulent transonic solutions with wide regions of separated flow.

The main drawback of the method remained its relatively slow convergence. To accelerate the convergence, a simplified multilevel scheme was used in [7], where the computations on each successively finer level used as initial guesses solutions interpolated from a coarser grid. But in this approach, referred to henceforth as the *grid-sequencing* method, the coarser grids were never visited again, so the usual multigrid convergence rates were not achieved. Moreover, because of extensive use of local grid refinements (which may cover only the boundary layer regions, for example), coarser grid feedback is necessary to get a correct overall solution. In order to perform large-scale computations employing millions of grid points, it was crucial to improve the efficiency of the method, while still retaining its high accuracy. Unfortunately, a straightforward implementation of the multigrid strategy employing FAS (full approximation scheme [10]) in conjunction with ENO discretization was not satisfactory even for inviscid solutions, and it failed to converge for high-Reynolds solutions of the Navier–Stokes equations. This is partly due to the very nonsmooth solutions (with shocks and boundary layers) and to the anisotropies (which are due to grid-stretching near boundaries). But even for smooth solution fields, ENO discretization does not produce stencils for which efficient smoothers can be constructed. Depending on the local smoothness properties of the fields, ENO may produce central-difference stencils or even downstream-biased stencils (if the flux is smoother in the downstream region than upstream). Additional problems arise as small changes in the solution field lead to a flip-flop behavior of a stencil, resulting from the nonlinear dependence of the discretization on the solution. This prevents the standard direct multigrid approach from succeeding with ENO. (See also associated problems in multigrid solution of flows at high-Reynolds numbers and recommended solution methods in [11, 12].)

To overcome the difficulties mentioned above we preferred an approach where the target discretization is different from that used in the relaxation process of the multigrid cycle. With this end in view, the solver of [5–7] was changed to be based on a defect correction multigrid approach. We employ a first-order-accurate driver, which is relatively easy to invert, and a high-order ENO defect correction.

We accelerate the convergence of the defect correction process by using stencil-dependent damping to the defect correction, employing damping parameters determined by a simple one-dimensional a priori analysis and numerical tests. This approach leads to a faster and smoother convergence.

The resulting multigrid method is stable and convergent. It retains the high accuracy of the ENO method of [5–7] and allows performing high-resolution computations incorporating local grid refinements by using the necessary multigrid feedback from coarser grids. Although the method does not achieve the so-called textbook multigrid efficiency typical to elliptic problems, only a comparatively small number of multigrid cycles is needed to reduce the error below the level of truncation errors. From the aerodynamic perspective, this means that the method yields at least three significant figures in lift and drag coefficients allowing accurate estimates of sensitive flow characteristics on practical mesh densities to be obtained. The results include three benchmarks:

1. Inviscid flow over ONERA M-6 on a set of grids with high aspect ratio cells.
2. Turbulent flow computation over the common test-case of ONERA M-6.
3. Turbulent flow computation over a transport-type cranked wing with highly cusped profiles, in flight conditions of high transonic flow, involving large regions of separated flow.

The above tests are compared with theory (item 1) and with wind-tunnel experiments (items 2 and 3). Multigrid versus grid-sequencing comparisons are given where appropriate.

The paper has the following structure: The governing equations and the discretization is given in Section 2. In Section 3 the multigrid defect-correction approach is described. The optimal damping and convergence analysis of the defect-correction process is given in Section 4. Extensive numerical results are given and analyzed in Section 5.

2. THE EQUATIONS AND DISCRETIZATION

The Navier–Stokes equations in Cartesian coordinates may be written in the form

$$\mathbf{q}_t + div\,\mathbf{C} = div\,\mathbf{V}, \tag{2.1}$$

where the tensor $\mathbf{C} = (\mathbf{f}, \mathbf{g}, \mathbf{h})$ represents the convection terms, the tensor $\mathbf{V} = (\mathbf{r}, \mathbf{s}, \mathbf{h})$ represents the viscous terms, $\mathbf{q} = (\rho, \rho\mathbf{u}, \rho\mathbf{v}, \rho\mathbf{w}, E)$ is the density, $(\mathbf{u}, \mathbf{v}, \mathbf{w})$ is the velocity vector, E is the energy, t is the time, $\mathbf{f}, \mathbf{g}, \mathbf{h}$ are the inviscid (convection) fluxes, and $\mathbf{r}, \mathbf{s}, \mathbf{t}$ are the viscous fluxes which depend in a nonlinear mode on $\mathbf{q}$.

The key point of the approximation scheme for the Navier–Stokes equations is the choice of discretization for the convective part of the spatial operator. To deal with practical aerodynamic configurations in the industrial environment the following requirements are to be met:

1. Applicability to 3D reasonably smooth grids not necessarily defined by mapping functions, but rather by more general sets of vertices.
2. Applicability to high aspect ratio grids typical to Navier–Stokes computations.
3. Ability to "coexist" with viscous terms without overriding them by artificial viscosity effects.
4. High accuracy on aerodynamic level including computation of sensitive flow characteristics such as drag.
5. Use of a minimal number of numerical parameters.
6. Robustness.
7. A high ratio of accuracy to computational work.

These requirements lead us to employ a low-dissipation scheme allowing good accuracy on relatively coarse grids. Theoretical considerations, supplemented by extensive numerical experiments, showed that the ENO-based scheme first introduced in [5–7], and briefly described in this section, possesses the above properties. In this work, the numerical scheme is incorporated in a multigrid framework by means of the defect-correction approach. This enhances the robustness of the method and substantially accelerates the computations allowing us to perform the large-scale calculations of complex 3D turbulent flows. The computational aspects of this approach are discussed in Sections 3 and 4.

2.1. *Spatial Approximation of Convection Terms*

We assume that the grid is structured, consisting of cells that form an (i, j, k) structure. By integrating over each cell separately we get a system of ODEs which can be solved by a time-stepping procedure.

For a particular cell (i, j, k) the approximation is assumed to be

$$\begin{aligned}(\Omega_{i,j,k}\mathbf{q}_{i,j,k})_t &+ [\mathbf{C}\cdot(S\mathbf{n})]_{i+0.5,j,k} - [\mathbf{C}\cdot(S\mathbf{n})]_{i-0.5,j,k} + [\mathbf{C}\cdot(S\mathbf{n})]_{i,j+0.5,k} \\ &- [\mathbf{C}\cdot(S\mathbf{n})]_{i,j-0.5,k} + [\mathbf{C}\cdot(S\mathbf{n})]_{i,j,k+0.5} - [\mathbf{C}\cdot(S\mathbf{n})]_{i,j,k-0.5} \\ &= [\mathbf{V}\cdot(S\mathbf{n})]_{i+0.5,j,k} - [\mathbf{V}\cdot(S\mathbf{n})]_{i-0.5,j,k} + [\mathbf{V}\cdot(S\mathbf{n})]_{i,j+0.5,k} \\ &- [\mathbf{V}\cdot(S\mathbf{n})]_{i,j-0.5,k} + [\mathbf{V}\cdot(S\mathbf{n})]_{i,j,k+0.5} - [\mathbf{V}\cdot(S\mathbf{n})]_{i,j,k-0.5}, \qquad (2.2)\end{aligned}$$

where $\Omega_{i,j,k}$ is the cell volume, $\mathbf{q}_{i,j,k}$ is some mean value of $\mathbf{q}$ over the cell, and S is the area of a cell side surface. Half-indices indicate from which side of the cell the flux (in square brackets) is taken as we now describe.

Fluxes with half-indices are approximated by a one-dimensional interpolation from nearby cell centers. That is, fluxes with subscripts $i+\frac{1}{2}, j, k$ and $i-\frac{1}{2}, j, k$ are approximated by fluxes at the cell centers with the same j and k and so on. A difficulty is introduced by the use of a staggered grid (with $\mathbf{q}$, $\mathbf{C}$ defined at cell centers and the associated fluxes on the cell sides, as opposed to the case of grids defined by an analytic mapping where the *curvilinear* fluxes are well defined at the cell centers). The interpolation operator must possess the following properties:

The approximation property. When the grid is smooth, it must approximate well a corresponding curvilinear flux in a mapping-defined system of coordinates.

The consistency property. A constant-field solution is interpolated exactly.

These properties are ensured, e.g., by choosing the interpolation operator I in the form

$$[\mathbf{C}\cdot(S\mathbf{n})]_{i+0.5,j,k} = I\{\mathbf{C}_{l,j,k}\cdot(S\mathbf{n})_{i+0.5,j,k}\} \quad l = i, i+1, i-1, \ldots, \qquad (2.3)$$

with the direction vector frozen in the interpolant. The specific choice of the (nonlinear) operator I is described next.

2.2. *Upwind-Biased and ENO Implementation*

The upwind-biased scheme actually used in the relaxation process employs only a one-point template for each characteristic flux interpolation, chosen according to the sign of the corresponding eigenvalue. The characteristic decomposition is applied at half-indexed points of the grid. An approximate Jacobian in the appropriate direction is introduced, and fluxes in the right-hand side of Eq. (2.3) are projected into local characteristic fields.

The ENO approach is implemented by choosing a template in the right-hand side of Eq. (2.3) according to local characteristics and smoothness of the fluxes, which may change with iterations. An ENO interpolation template (typically consisting of three points in this work) is determined separately in each field, primarily according to the sign of the corresponding eigenvalue and then according to the smoothness of the projected fluxes [4–6]. The interpolated characteristic fluxes are projected back to get the Cartesian ones.

In the framework of the present method the ENO procedure mentioned above is applied only for the defect-correction calculation a very limited number of times (roughly equal to the number of multigrid cycles), and most of the computational work is performed using a relatively cheap upwind biased relaxation (see also Section 3.)

Remark. In the case of an eigenvalue λ changing sign between indices I and $I+1$, the corresponding flux f is split into two fluxes $f+$ and $f-$ such that

$$\begin{aligned}(f+)+(f-) &= f\\ (f+)-(f-) &= \max\{|\lambda_I|, |\lambda_{I+1}|\}\, Proj_\lambda(\mathbf{q}),\end{aligned} \tag{2.4}$$

and the procedure is applied separately on $f+$ and $f-$ (so-called entropy fix). Note that there is no need for any artificial numerical parameters in Eq. (2.4).

2.3. *Approximation of Viscous Terms*

Natural finite differences are used to approximate the first derivatives along the local grid coordinates. The Cartesian derivatives are obtained by combining the above derivatives in a way which ensures exactness for a linearly changing flow-field.

2.4. *Time-Marching*

A three-stage Runge–Kutta scheme is applied in a TVD preserving form [4] with theoretical CFL $= 1$. To accelerate the convergence to steady state, explicit residual smoothing is applied. It allows CFL numbers of about 1.5 (instead of 0.75 which is used in practice without the residual smoothing) for subsonic and transonic flows in the case of ENO $= 3$ and up to 2 for the upwind biased relaxation. Actually, the latter is used everywhere except in the computation of the defect correction. For steady state computations, local time steps are used based on local eigenvalues calculated separately for inviscid and viscous operators.

2.5. *Sensitive Faces, Cells, and Use of a Linearly Stable Template*

In practice, to save substantial computational effort without appreciable loss of accuracy, a fixed linearly stable template is applied everywhere except on "sensitive" faces where the variable ENO template is used. The cell face is called sonic if one of the sonic eigenvalues changes sign across the face. The face is called sensitive if it belongs to the one-dimensional neighborhood of a sonic cell face. The neighborhood is measured by the number of points in the ENO template-1.

The notion of sensitive face is also used in the damping coefficients technique (see Section 4). A cell is called sensitive if at least one of its faces is sensitive, and different damping coefficients may be used in sensitive and nonsensitive cells. This allows for improvement of the convergence rate (see Section 5.4). The values of damping coefficients used in practice are 0.6 for sensitive cells and 1.1 for nonsensitive cells.

3. MULTIGRID DEFECT CORRECTION APPROACH

The code is embedded in the framework of the multigrid method; that is, the grids are arranged in hierarchical levels, starting from a coarse level (grid) which typically contains a single grid, and then refining it so that each grid contains the next-level refinement geometrically. Local refinements are allowed and are used in practical computations.

Multigrid algorithms were originally developed as solvers for discretized linear elliptic boundary-value problems, but sophisticated algorithms for nonlinear fluid-flow problems

were already developed two decades ago (see [19] and numerous references therein). The multigrid algorithm or "cycle" is a generalization, by some recursion, of the two-grid cycle. The latter is composed of two stages, an error-smoothing process and a coarse-grid correction stage. Error smoothing is performed by a (usually) local and computationally inexpensive relaxation process, such as Gauss–Seidel relaxation. The aim of this stage is to reduce error modes that are oscillatory relative to the grid. The equations for the error are then approximated and solved on a coarser grid, and the resulting correction is interpolated and added to the fine-grid solution to obtain an improved approximation. The so-called full-approximation scheme (FAS) [10] is a generalization of this basic algorithm which can handle nonlinear problems directly, as well as facilitating the incorporation of local refinement and other advanced techniques. The multigrid cycle is embedded in a grid-sequencing algorithm (known as full multigrid—FMG), which supplies a good initial approximation to the fine-grid solution by first solving the problem on a coarser grid and interpolating the solution to the fine grid.

Multigrid methods have been used successfully for solving hard problems of fluid dynamics by a very large number of researchers and practitioners; see for example [15–18]. However, we are not aware of successful applications of multigrid methods in conjunction with ENO discretization for difficult problems.

Previously [5–7], only the simple grid-sequencing procedure was employed. That is, the computation on each successively finer level used results interpolated from the coarser level as an initial guess. But the coarser grids were never revisited, so although this method was useful compared to single-grid computations, it did not exhibit the required multigrid acceleration. Moreover, because of the use of local grid refinements, coarser grid feedback is necessary in order to get a correct overall solution. That is, the mutual effect of the solution in regions where the fine grid is not employed and in regions where it is employed must be taken into account. The method and the corresponding computer code are ultimately intended to deal with complex aerodynamic configurations, similarly to [13]. Therefore, it is crucial to improve the efficiency of the method without compromising accuracy. As noted in Section 1, direct application of the multigrid algorithm with ENO is inefficient (sometimes nonconvergent). Instead, we resort to a method where a simple stable scheme is used for relaxation within the multigrid algorithm. The ENO discretization is employed to correct the defect in the equations resulting from the less accurate discretization. This general approach has often been used before for fluid-flow problems, with and without multigrid; see, e.g., [21–23].

In its basic form the defect correction approach is defined by an iterative process for a given problem

$$L\mathbf{u} = \mathbf{F}, \tag{3.1}$$

which can be written as

$$L_1\mathbf{u}^{(n+1)} = \mathbf{F} - \left[L_2\mathbf{u}^{(n)} - L_1\mathbf{u}^{(n)}\right]. \tag{3.2}$$

Here, $\mathbf{u}$ and $\mathbf{F}$ are the solution and the given forcing term, respectively, n is the iteration number, L is a (possibly nonlinear) operator, L_2 is typically a high-order operator approximation (ENO in our application) to L, and L_1 is an approximation to L that can be inverted efficiently by multigrid techniques. Thus, a defect correction, representing the difference

between the values of operators L_1 and L_2 applied to the current solution field, is added as a forcing term to the right-hand side of the equations, and the actual relaxation process is performed using a stable and easy-to-invert operator L_1. In this work, operators L_1 and L_2 only approximate the convection part of the equations differently, and the viscous terms approximated as described above are added to the left-hand side of Eq. (3.2). The term L_1 is chosen as a low-order upwind-biased operator, with *characteristic fluxes* interpolated by only a *one-point stencil* determined (in each characteristic field) according to the sign of the corresponding eigenvalue. The term L_2 is the ENO operator described above. It typically employs three-point variable stencils for flux approximation. The defect correction is applied only on multigrid levels which contain ultimately refined local grids; on other levels the relaxation process is simply driven by the low-order operator L_1. Thus, when no local refinements are used, the defect correction is applied only on the finest level.

A potentially attractive development of ENO discretization is WENO (weighted ENO; see [8, 9].) In this approach, a weighted average of interpolated fluxes is employed, rather than only interpolating from the neighboring region where the flow is smoothest. The analysis given in the following sections gives rise to hopes that WENO schemes (which are a combination of stencils that may be produced by ENO) may also be handled effectively by the multigrid defect-correction framework. However, in our present application, WENO schemes are unlikely to provide a significant advantage, since, as noted above, we use ENO only at sensitive points where a discontinuity occurs within the span of the stencil. At these points WENO stencils emulate ENO ([9], p. 18), because of the large discrepancy in smoothness among the cells spanned by the stencil. Also, more research seems to be required to establish the proper WENO weightings, especially in the case of 3-D industrial flows.

4. OPTIMAL DAMPING AND CONVERGENCE OF THE DEFECT-CORRECTION PROCESS

We present here a simple convergence analysis for the defect-correction process. We first generalize the defect-correction algorithm slightly (but effectively) by introducing a damping parameter, ω. Accordingly, we modify Eq. (3.2) as

$$L_1\mathbf{u}^{(n+1)} = L_1\mathbf{u}^{(n)} + \omega\left[\mathbf{F} - L_2\mathbf{u}^{(n)}\right]. \tag{4.1}$$

Note that for $\omega = 1$ Eq. (4.1) is reduced to (3.2). For $\omega < 1$ the correction is damped, while $\omega > 1$ represents over-correction. Usually, we shall not distinguish between these two cases and use the term "damping" for any ω.

To analyze the convergence properties of the damped defect-correction process we denote the converged solution by $\bar{\mathbf{u}}$ (that is, $L_2\bar{\mathbf{u}} = \mathbf{F}$) and subtract from Eq. (4.1) the trivial equation

$$L_1\bar{\mathbf{u}} = L_1\bar{\mathbf{u}} + \omega[\,\mathbf{F} - L_2\bar{\mathbf{u}}]. \tag{4.2}$$

Suppose that L_1 and L_2 are linear operators, and let $\mathbf{e}^{(n+1)} = \mathbf{u}^{(n+1)} - \bar{\mathbf{u}}$ and $\mathbf{e}^{(n)} = \mathbf{u}^{(n)} - \bar{\mathbf{u}}$ denote the errors after iteration $n+1$ and iteration n, respectively. We thus obtain

$$L_1\mathbf{e}^{(n+1)} = [L_1 - \omega L_2]\mathbf{e}^{(n)}. \tag{4.3}$$

We can use Eq. (4.3) to prove convergence of the residual $L_1\mathbf{e}^{(n)}$ in certain cases, and also to optimize ω.

Consider for example the case where L_1 and L_2 are the standard first-order-accurate and second-order-accurate upwind discretizations of the convection operator in 1D,

$$\begin{aligned} L_1 u_i &= f_i - f_{i-1}, \\ L_2 u_i &= \frac{3}{2} f_i - 2 f_{i-1} + \frac{1}{2} f_{i-2} \\ &= \frac{3}{2} L_1 u_i - \frac{1}{2} L_1 u_{i-1}, \end{aligned} \tag{4.4}$$

where $f = f(u)$ is some linear flux (for example $f(u) = u$.) Substituting these operators into Eq. (4.3) yields

$$L_1 e_i^{(n+1)} = \left(1 - \frac{3\omega}{2}\right) L_1 e_i^{(n)} + \frac{\omega}{2} L_1 e_{i-1}^{(n)}, \tag{4.5}$$

and hence, using the maximum norm,

$$\left\| L_1 \mathbf{e}^{(n+1)} \right\| \le \left(\left| 1 - \frac{3\omega}{2} \right| + \left| \frac{\omega}{2} \right| \right) \left\| L_1 \mathbf{e}^{(n)} \right\|. \tag{4.6}$$

We find that the amplification factor of the residual norm is bounded from above by

$$\mu = \frac{\left\| L_1 \mathbf{e}^{(n+1)} \right\|}{\left\| L_1 \mathbf{e}^{(n)} \right\|} \le \left| 1 - \frac{3\omega}{2} \right| + \left| \frac{\omega}{2} \right|. \tag{4.7}$$

Now, if we choose the standard $\omega = 1$, we get $\mu \le 1$, which implies that the defect-correction process may stagnate (as indeed it does in this case [20]). But if we employ the optimal damping factor $\omega = 2/3$, we obtain $\mu = 1/3$, implying extremely fast convergence of nearly an order of magnitude per every two iterations.

In contrast to this example, discretizations that are mostly or only of central-difference type are likely to exhibit slow convergence in defect-correction iterations, as well as direct multigrid iterations, because of their small h-ellipticity measures. An h-elliptic finite difference operator is one for which *any* error which is oscillatory relative to the discretization grid (i.e., varies significantly over a small number of mesh-cells) produces a relatively large residual. (See, e.g., [19] for a quantitative definition in the framework of Fourier local-mode analysis.) Central-difference advection operators are not generally h-elliptic. Therefore, as we now show, convergence rates cannot be improved significantly by damping.

Central-difference discretizations for linear convection in 1D can be written in the form

$$L_2 u_i = \sum_j a_{i,j} \frac{f_{i+j} - f_{i-j}}{2j}, \tag{4.8}$$

where the sum is taken over the span of the stencil, and $\sum_j a_{i,j} = 1$. Here, $f(u)$ is again some linear flux. Consider an oscillatory error of the form

$$e_i = (-1)^i \phi_i,$$

where ϕ is some function that is smooth relative to the grid. That is, ϕ (hence also $f(\phi)$) undergoes very little relative variation over the span of the discretization stencil, and therefore

$$\frac{\|L_2\phi\|}{\|f(\phi)\|} = \epsilon(\phi) \ll 1.$$

Since, for all i, j, $(-1)^{(i+j)} = (-1)^{(i-j)}$, it follows from from (4.8) that $\|L_2\mathbf{e}\| \sim \|L_2\phi\|$. On the other hand, for the first-order upwind scheme we have

$$|L_1 e_i| = |f(e)_i - f(e)_{i-1}| = |f(\phi)_i + f(\phi)_{i-1}|,$$

and therefore, $\|L_1\mathbf{e}\| \sim \|f(\phi)\|$, because of the smoothness of $f(\phi)$ relative to the grid. We conclude that for such oscillatory errors,

$$\frac{\|L_2\mathbf{e}\|}{\|L_1\mathbf{e}\|} = O(\epsilon).$$

Hence, by Eq. (4.3), the defect-correction iteration yields for such errors

$$\frac{\left\|L_1\mathbf{e}^{(n+1)}\right\|}{\left\|L_1\mathbf{e}^{(n)}\right\|} \geq 1 - \omega O(\epsilon).$$

Since an obvious requirement for convergence is $\omega < 2$ (because, for errors that are smooth relative to the grid, $L_1\mathbf{e} \approx L_2\mathbf{e}$, by consistency), we conclude that such oscillatory errors converge slowly in the defect-correction process regardless of ω. At best, ϵ^{-1} iterations are required to reduce the error by an order of magnitude or so. Similarly, since smoothing of all oscillatory errors (i.e., such that are not resolved by the coarser grid) is essential for multigrid convergence as well, central-difference discretizations do not lend themselves to direct application of multigrid techniques for precisely the same reason.

4.1. *Optimal ω for the ENO Operator*

The ENO method is inherently nonlinear, and the resulting discretization stencils depend on the current approximation to the solution. The efficiency of the defect-correction algorithm—and the optimal damping factor—depend on the stencils employed both for the target discretization and the driver. Hence, it is somewhat solution-dependent. However, in our code we actually use ENO only near sensitive regions in the domain where sonic eigenvalues change sign (see Section 2.5). In most parts of the domain we save computational cost with little or no loss of accuracy by employing a linear third-order scheme in which the flux is interpolated from one downstream and two upstream points. In the linear 1-D scalar case, assuming for simplicity a positive coefficient, the flux difference at cell i is approximated by

$$L_2 u_i = \frac{1}{3}(f_{i+1} - f_i) + \frac{5}{6}(f_i - f_{i-1}) - \frac{1}{6}(f_{i-1} - f_{i-2}), \tag{4.9}$$

while the driver again approximates the flux difference by the simple first-order upstream scheme L_1 of Eq. (4.4). Employing the same procedure as above, we find the bound on the

residual convergence factor to be

$$\mu \le \left|\frac{\omega}{3}\right| + \left|1 - \frac{5\omega}{6}\right| + \left|\frac{\omega}{6}\right| = \left|\frac{\omega}{2}\right| + \left|1 - \frac{5\omega}{6}\right|. \tag{4.10}$$

We discern that in the 1-D linear case the residual convergence factor of the defect-correction process with no damping ($\omega = 1$) is a satisfactory $\mu = 2/3$. This can be improved slightly by over-correction, the optimal ω being $6/5$, yielding $\mu = 0.6$. In practice, for the full nonlinear system, we found slightly better behavior if we used $\omega = 1.1$, rather than 1.2, presumably because the over-correction excites some nonlinear modes.

In sensitive regions many different stencils are possible, and for some cases (at sonic points) the driver itself can vary. But for two common cases, μ is as in Eq. (4.10), which we denote by μ_1. At the other extreme, for purely one-sided stencils, the residual convergence factor is bounded by

$$\mu_2 \le \left|\frac{\omega}{3}\right| + \left|\frac{7\omega}{6}\right| + \left|\frac{11\omega}{6} - 1\right| = \left|\frac{9\omega}{6}\right| + \left|\frac{11\omega}{6} - 1\right|. \tag{4.11}$$

Since either of these convergence factors is possible, we choose ω which will minimize $\max(\mu_1, \mu_2)$. The optimal choice for μ_2 is $\omega = 6/11 \approx 0.545$, yielding $\mu_2 \le 9/11$. As it happens, this choice of ω also yields $\mu_1 \le 9/11$, obtained by substituting $\omega = 6/11$ into Eq. (4.10). So the optimal ω seems to be $6/11$ under this worst-case analysis (because any other choice would increase the bound on μ_2.) However, this view is a bit too pessimistic for a somewhat subtle reason: μ_2 corresponds to one-sided stencils, say, purely upstream. But ENO will "pick" a purely upstream stencil only if the current flux differences are smoother in two consecutive upstream locations than in the neighboring downstream location. On the other hand, the bound for μ_2 given by Eq. (4.11) is sharp only if the flux-differences of the error at these two upstream locations are of different sign. But this means that the upstream error is in fact oscillatory, so ENO is very unlikely to produce this stencil when the worst-case conditions exist, at least while the error is large enough to affect the stencil. If we assume that the two neighboring upstream (or, analogously, downstream) flux-differences are of the same sign whenever this stencil occurs, we obtain

$$\mu_2 \le \left|\frac{5\omega}{6}\right| + \left|\frac{11\omega}{6} - 1\right|, \tag{4.12}$$

and the optimal choice for minimizing $\max(\mu_1, \mu_2)$ is then $\omega = 2/3 \approx 0.667$, yielding a residual convergence factor bound of $7/9$. In practice we found that using $\omega = 0.6$ yielded a good compromise between these two choices, and all the results we present use this value at sensitive points. We remark again that other stencils are also possible, for which the computation of the optimal ω is far less straightforward. It appears, however, that the above are the extreme cases.

Of course, convergence in 1D does not ensure convergence of the full three-dimensional problem, but it is a necessary condition. Also, it provides a good estimate of the convergence behavior in regions where the flow is nearly aligned with the grid, or nearly so, which typically occurs in a large part of the domain. Thus, these are encouraging results, and we indeed found that by following the guidelines of this analysis we obtained satisfactory convergence behavior for complicated three-dimensional flows as we describe below.

We conclude this section by remarking that an alternative to damping is the approach of recombining iterants, employing some acceleration method that is suitable for nonlinear problems. We chose not to employ such methods mainly because of the additional storage requirements. We believe, however, that employing such methods, especially in a spatially dependent way as suggested in [24] is likely to improve the convergence rates with little computational overhead (but nonnegligible additional memory).

5. RESULTS

Previously reported results [5–7] showed good accuracy on relatively coarse grids. They also exhibited good flow discontinuity capturing capacity of the ENO method without any need for numerical parameters which are associated with either explicit or implicit artificial viscosity. The objective of the present verification study was to check the ability of the modified method to allow (due to its multigrid structure) the improved accuracy of the calculations of aerodynamic parameters by employing additional refined grids with (optionally) local refinements. Solutions for transonic, turbulent flow over different configurations in flight conditions where viscous effects are significant were obtained. In these computations the effects of turbulence are modeled through an eddy-viscosity hypothesis with the Baldwin–Lomax turbulence model [25] used for turbulence closure.

An accuracy and robustness check was performed by solving the Euler equations with the new method on the set of grids designed for *viscous* computations, possessing much higher aspect ratio of computational cells than in conventional Euler computations. This allowed the verification of the robustness of the method in demanding conditions and the companson of the computed pressure drag values to the theoretical ideal induced drag.

The next series of computations were performed with the turbulent flow over the ONERA M-6 wing at free-stream Mach number $M_\infty = .84$ and angle of attack $\alpha = 3.06^\circ$ ($\mathrm{Re} = 11.7 \times 10^6$). This case has been the subject of numerous studies in the past with reliable surface pressure measurements available.

Additional computational tests address the flow over a cranked and twisted transonic wing with highly cusped profiles, typical of modern business jets. Because of these physical characteristics, transonic flow over this wing is complicated, and, because of thick boundary layers, computations performed with the inviscid (Euler) equations are almost irrelevant. The solutions presented here possess the normal spacings at the wing surface, keeping $y+$ of about 1.5–2.5 on the finest meshes employed in order to allow reliable representation of viscous effects.

5.1. *Robustness and Accuracy of the Method: Theoretical Check*

An interesting example, which enables us to verify the accuracy of the method, is obtained by solving the Euler equations on so-called Navier–Stokes grids. Such grids have much higher aspect ratio of cells than the conventional "Euler grids" (which are not supposed to resolve boundary layers). On the other hand, a discretization scheme approximating the convection operator is less dissipative in the absence of viscous terms. The accuracy of such computations reflects the ability of the grid to resolve accurately the convection terms of the Navier–Stokes equations. In the case of inviscid subsonic flow over a symmetric wing, the computed pressure drag may be compared to the theoretical ideal induced drag. It equals zero at zero angle of attack. The multigrid defect-correction method (DC) was applied to

TABLE I
Comparison Between Computed and Theoretical Pressure Drag for ONERA M-6 Wing at M_∞ = 0.60

Angle of attack (degrees)	C_D (theory)	C_D (DC)
0	0.0000	0.0001
1	0.0005	0.0006
2	0.0019	0.0020
3	0.0042+	0.0044

Note. Inviscid computations were on grids with high aspect ratio of cells. The suffix "+" means that at $\alpha = 3^\circ$, the flow possesses a supersonic pocket which apparently accounts for an additional 0.0001 discrepancy between computed and theoretical values.

the inviscid flow over the ONERA M-6 wing on the set of grids normally used for the Navier–Stokes computations (given in Section 5.2) at $M_\infty = .60$, with $\alpha = 0^\circ, 1^\circ, 2^\circ, 3^\circ$. The runs exhibited good convergence (just a few multigrid cycles yield 3 or 4 significant digits in aerodynamic coefficients). Table I compares the computed drag coefficients with the theoretical values.

Table II presents the asymptotic convergence of aerodynamic coefficients at $M_\infty = .60$, with $\alpha = 3^\circ$. The ultimately resolved grid (at level 4) contained $176 \times 64 \times 32$ cells. All the computations of Table II used the three-point ENO template at the finest level employed.

5.2. *ONERA M-6 Wing*

Pressure coefficients computed by the prototype ENO method [6] were in close agreement with the experiments for the case ($M_\infty = .84, \alpha = 3.06^\circ$) along the entire wing span. Good shock-capturing capability was demonstrated and the results were found to be very close to those exhibited by other high-accuracy computations. These computations used relatively coarse grids containing $44 \times 16 \times 8$, $88 \times 16 \times 16$ points (in the streamwise, normal to surface and spanwise directions, respectively) and a subset of a finer grid $176 \times 32 \times 16$ (which roughly covered the boundary-layer region) as a local refinement. A partial view of the grid is given in Fig. 1. The computation in [6] (which used the simple grid-sequencing approach) yielded lift and drag coefficients of $C_L = .268$ and $C_D = .0178$, respectively.

TABLE II
Asymptotic Behavior of Aerodynamic Coefficients for ONERA M-6 Wing at M_∞ = 0.60

# of MG levels	C_L	C_D
1	0.2201	0.0083
2	0.2183	0.0057
3	0.2222	0.0046
4	0.2219	0.0044

Note. Inviscid Computations were done on grids with high aspect ratio of cells.

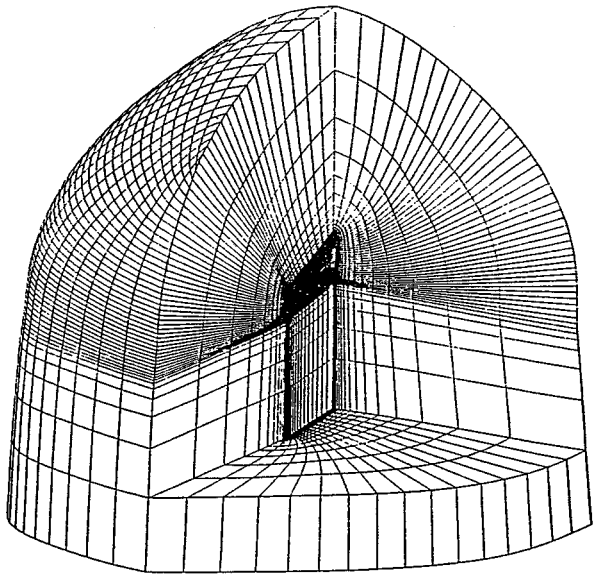

FIG. 1. Partial view of C-O mesh for ONERA M-6 wing.

These figures closely matched previously published results by other authors on substantially finer computational grids [6].

To test the ability of the modified method to produce improved accuracy of aerodynamic estimates, this case was rerun. One series of computations was performed with the old (grid sequencing) and new (defect correction) methods, using the set of grids of [6], except for the finest grid which was extended to include the entire computational domain, in order to provide a reference for comparison. Both computations gave identical aerodynamic coefficients $C_L = .270$ and $C_D = .0174$ and practically identical pressure distributions. The code of [6] used the three-point ENO stencil on all three levels, while the present method employed a one-point upwind-biased scheme on all multigrid levels with a three-point ENO defect correction on the finest level. It may be concluded that:

1. In the absence of local refinements both methods produce the same numerical results (though of course the computation by the new method is much faster).
2. The old method is less accurate when applied to the case were local refinements are involved.

The next step was to rerun the exact set of grids used in [6] (with local refinement on the finest level) by the new method. The results were the same as those achieved by both methods on the set with a full fine grid. This suggests that the multigrid defect-correction method properly applied to reduced grids (local refinements) essentially retains the accuracy achieved on full fine grids.

To verify the asymptotic behavior of the method, a fourth level, containing a local refinement (in the direction normal to the surface) of the third-level grid, was added. The new set of grids was used twice by the multigrid method. In the first run, the defect-correction strategy was applied on the third and fourth levels since the third level contains ultimately refined regions. The second run employed the defect correction on the fourth level only and, to ensure the accuracy, the relaxation scheme on the third level was switched from

TABLE III
Effect of Grid Density on Aerodynamic Coefficients
(M_∞ = .84, α = 3.06°)

# of Levels	C_L	C_D pressure	C_D friction
3	0.270	0.0125	0.0049
4	0.269	0.0119	0.0051

the upwind-biased to the three-point ENO. Both computations gave almost identical pressure distributions with $C_L = .269$ and $C_D = .0170$ in both cases. Table III summarizes the values of aerodynamic coefficients for three- and four-level multigrid.

In Fig. 2 the computed surface pressure coefficients (taken from the finest grid) are compared with wind-tunnel experiment at the station $2y/b = .44$. In Fig. 3 the third-level results are presented at the same span station which were taken (1) from the three-level computation and (2) from the four-level computation. It is interesting to note that an almost imperceptible change in surface pressure distributions resulting from the refinement, which is typical for the whole wing span, has an appreciable impact on the pressure drag.

5.3. *Multigrid Performance of the Method: Turbulent Transonic Flow over a Transport-Type Cranked Wing*

The goal of this study is to estimate the performance of the new method by applying it to a glove-like wing with twisted and cusped profiles. At the transonic flight conditions, the case is representative of a flow which is highly influenced by shock–boundary layer

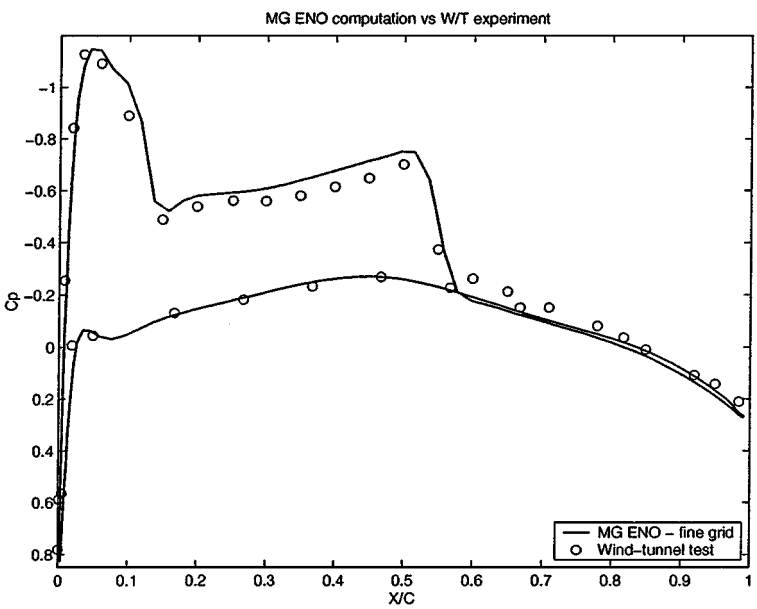

FIG. 2. Comparison of computed pressure distributions and wind-tunnel experiment. Four multigrid levels were employed, with the finest grid covering only the boundary-layer region (local refinement). In the experiment, $2y/b = 0.44$. In the computation $2y/b = 0.47$, which was the closest pressure location defined in the computation.

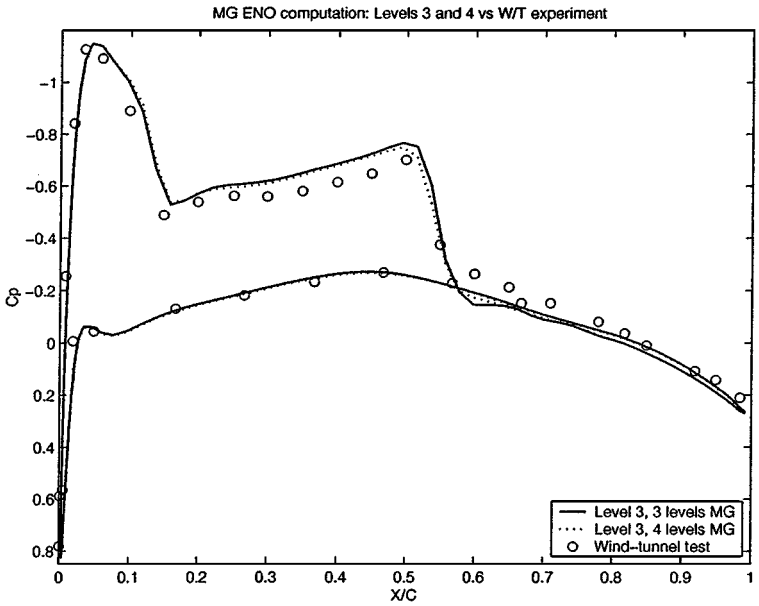

FIG. 3. Comparison of two computed pressure distributions and wind-tunnel experiment. The results using three full-domain multigrid levels are compared to those employing also an additional locally refined grid (in the boundary-layer regions). The results shown are from the third computational grid, with $2y/b = 0.44$ (same as the experiment). This accounts for the slightly better rear-shock fit than seen in Fig. 2.

interaction. This usually slows down the convergence of numerical schemes. The geometry of the wing with previous numerical experiments are given in [6, 7]. The results indicated good accuracy. The ability of the code to produce reliable results for substantially different flight conditions is demonstrated in Figs. 4 and 5.

The convergence of the grid-sequencing code was, however, slow. The present numerical experiment confirmed the ability of the new method to resolve properly the shock–boundary layer interaction by using the technique of local refinements. The results are similar to those achieved for the ONERA M-6 wing. To estimate the multigrid acceleration, which resulted from the use of the defect-correction method (DC), the results were compared to those achieved by the previously used grid-sequencing (GS) algorithm. Comparisons are presented at $M_\infty = .80$, $C_L = .53$ (which correspond to flight conditions higher than those of cruise). In this regime, a straightforward MG strategy (FAS) in conjunction with a usual ENO relaxation scheme fails even when it is applied to only two coarser levels. To demonstrate the convergence history of the computations, the lift, pressure drag, and skin-friction coefficients are presented in Tables IV, V, and VI, respectively, as a function of the computational work. In these tables, 1 "work unit" roughly corresponds to 15 iterations of the DC method. The integral norm of the density residuals is given in Table VII. The computation employed three multigrid levels with successive grids containing $44 \times 16 \times 8$, $88 \times 16 \times 16$, and $176 \times 32 \times 16$ computational cells in the streamwise, normal to surface, and spanwise directions, respectively.

Both computations ultimately produced almost identical results including the surface pressure distributions which are omitted here. It may be concluded from Tables IV–VII that the defect-correction multigrid method is about four times faster. For example, the accuracy of 0.5% in both lift and drag coefficients is achieved within less than one work unit by the

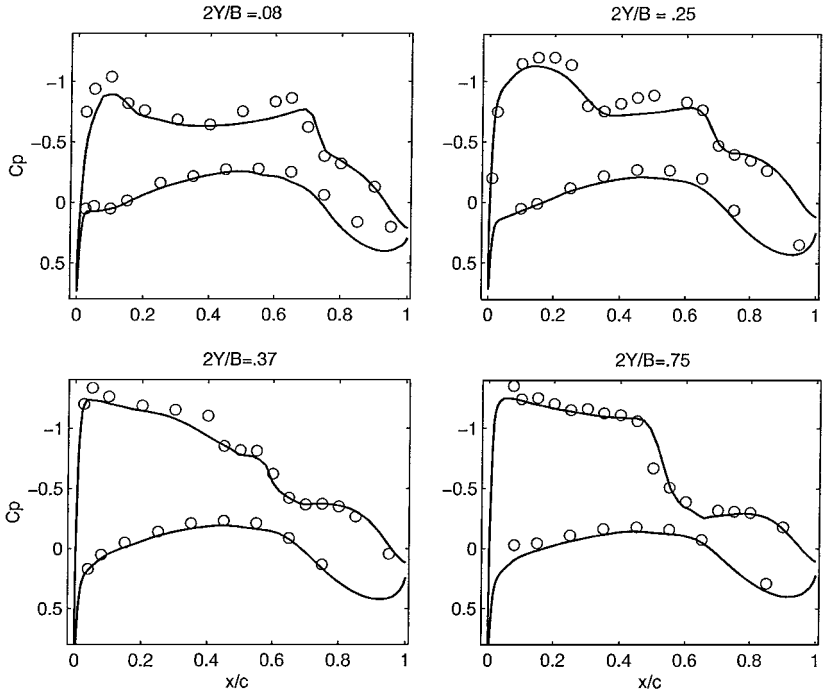

FIG. 4. Transport-type wing. Chordwise pressure distribution at different span stations. MG ENO computation versus wind-tunnel experiment. $M = .80$, $Re = 3.5 \times 10^6$, $\alpha = 1^\circ$. Solid lines represent computation and circles represent full aircraft W/T test.

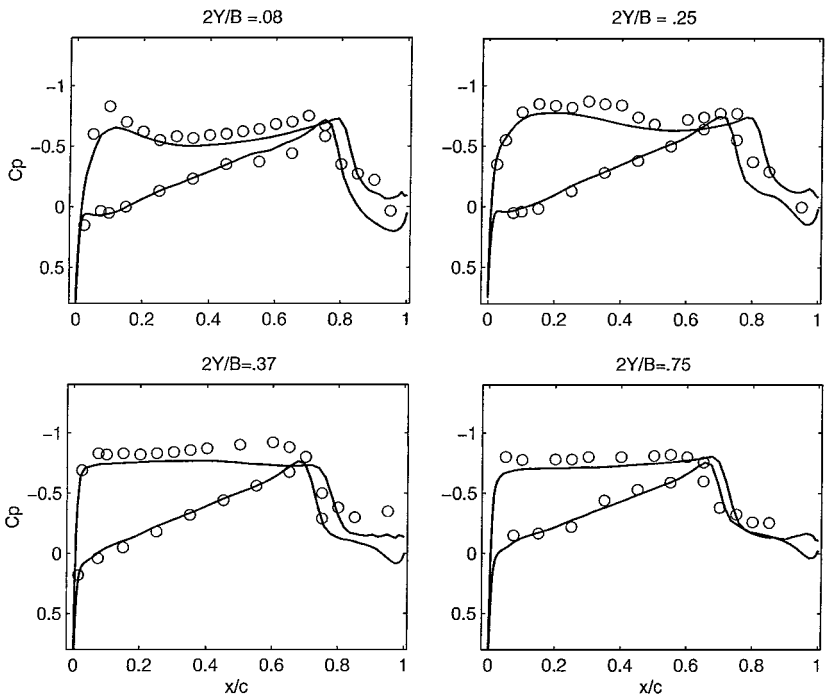

FIG. 5. Transport-type wing. Chordwise pressure distribution at different span stations. MG ENO computation versus wind-tunnel experiment. $M = .92$, $Re = 3.5 \times 10^6$, $\alpha = 1^\circ$. Solid lines represent computation and circles represent full aircraft W/T test.

TABLE IV
Convergence History of the Lift Coefficients Computed by the Previous (GS) and New (DS) Method

Work units	C_L (DC)	C_L (GS)
1	0.531	0.512
2	0.534	0.525
4	0.534	0.532
6		0.534

Note. Transport-type cranked wing, $M_\infty = .80, \alpha = 1.0^\circ$.

TABLE V
Convergence History of the Pressure Drag Coefficients Computed by the Previous (GS) and New (DS) Method

Work units	C_D pressure (DC)	C_D pressure (GS)
1	0.0231	0.0220
2	0.0232	0.0225
4	0.0232	0.0231
6		0.0232

Note. Transport-type cranked wing, $M_\infty = .80, \alpha = 1.0^\circ$.

TABLE VI
Convergence History of the Skin-Friction Coefficients Computed by the Previous (GS) and New (DS) Method

Work units	C_D friction (DC)	C_D friction (GS)
1	0.0052	0.0051
2	0.0052	0.0052
4	0.0052	0.0052
6		0.0052

Note. Transport-type cranked wing, $M_\infty = .80, \alpha = 1.0^\circ$.

TABLE VII
Convergence History of the Density Residual Computed by the Previous (GS) and New (DS) Method

Work units	Residual (DC)	Residual (GS)
1	$1.0e^{-7}$	$1.0e^{-6}$
2	$2.0e^{-8}$	$4.0e^{-7}$
4	$2.0e^{-9}$	$7.0e^{-8}$
6		$2.0e^{-8}$

Note. Transport-type cranked wing, $M_\infty = .80, \alpha = 1.0^\circ$.

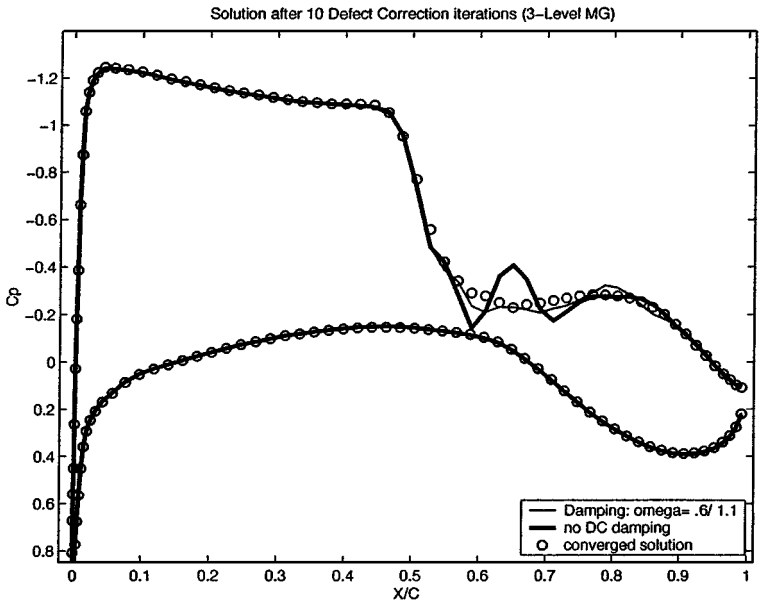

FIG. 6. Transport-type wing. Chordwise pressure distribution at the midsection of the outer wing. Solution after 10 defect-correction iterations (3-level MG).

DC method compared to four work units by the old method. Moreover, the new method exhibits almost monotonic convergence of the residuals while the old (GS) method exhibits a rather "wavy" behavior. Numerical experiments with additional wings showed that the above acceleration factor is often even higher than reported here. Wings of irregular form

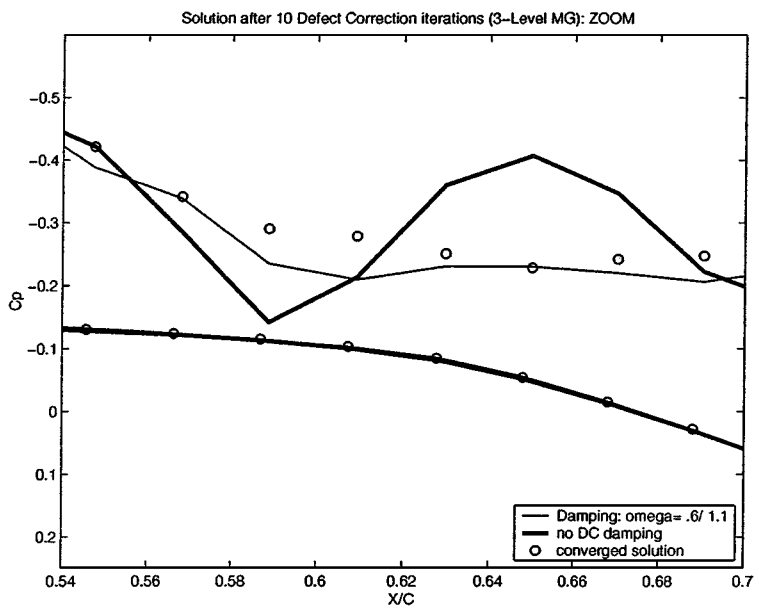

FIG. 7. Transport-type wing. Chordwise pressure distribution at the midsection of the outer wing. Solution after 10 defect-correction iterations (3-level MG): zoom.

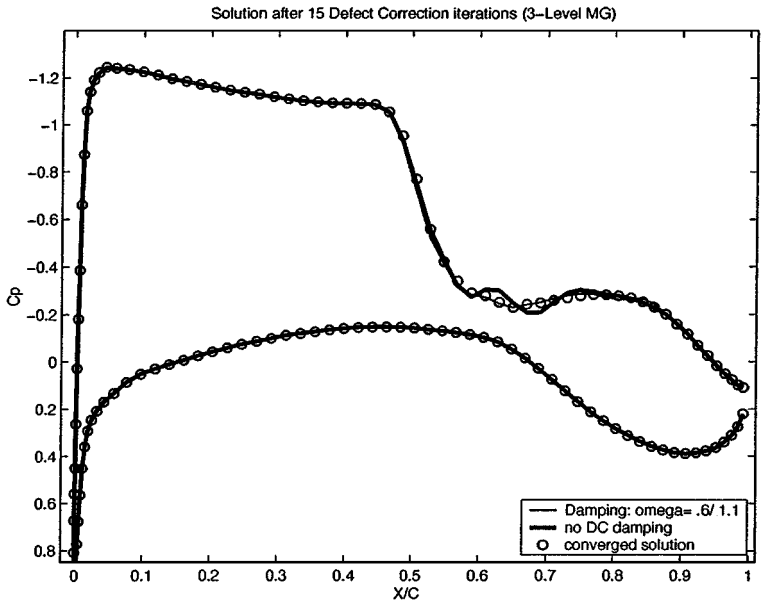

FIG. 8. Transport-type wing. Chordwise pressure distribution at the midsection of the outer wing. Solution after 15 defect-correction iterations (3-level MG).

enjoy higher rates of acceleration because of the use of the present method. Furthermore, the improvement is expected to be still greater as finer grids are employed, because the performance of the naive grid-sequencing scheme must deteriorate both in terms of the convergence rate and in terms of its accuracy if local refinement is used.

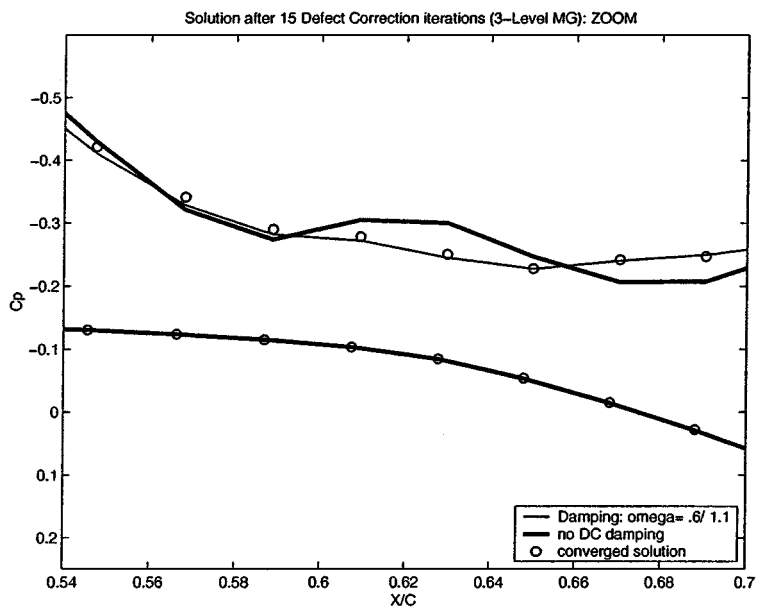

FIG. 9. Transport-type wing. Chordwise pressure distribution at the midsection of the outer wing. Solution after 15 defect-correction iterations (3-level MG): zoom.

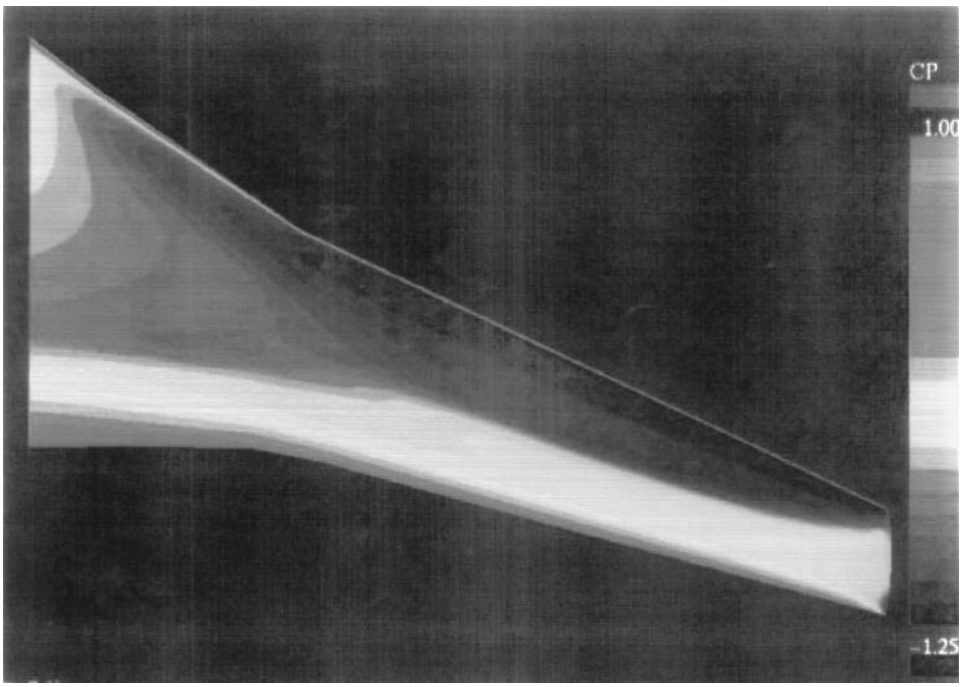

FIG. 10. Transport-type wing. Pressure distribution on the upper surface of the wing.

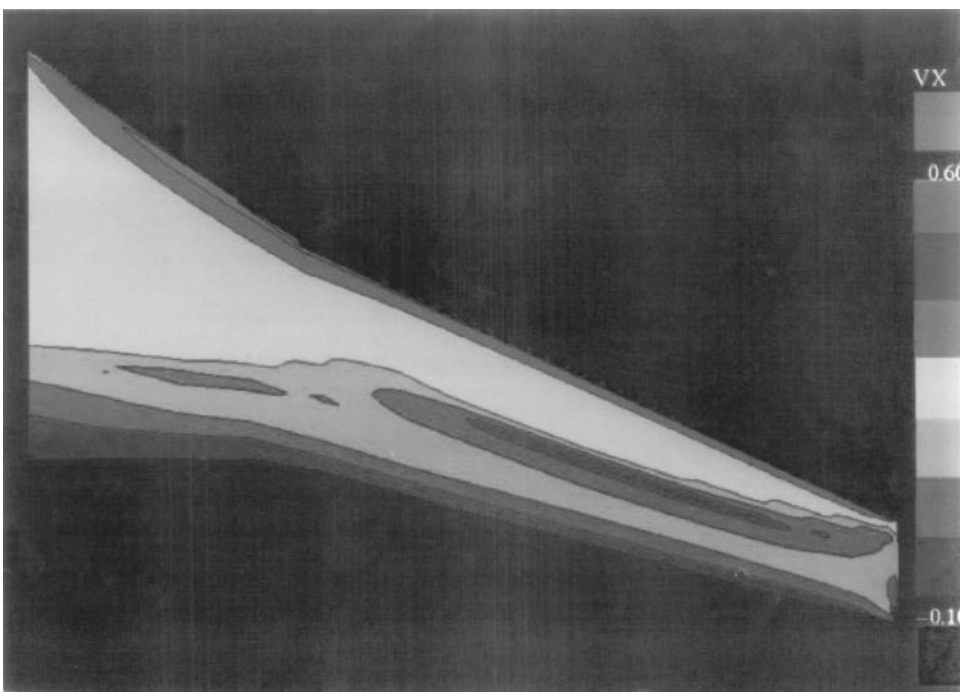

FIG. 11. Transport-type wing. Streamwise velocity VX contours just above the upper surface of the wing.

5.4. *Damped Defect Corrections*

Here we present the computational results with the use of the damping technique which was described in Section 4. We use the same aerodynamic configuration and flight conditions as in Section 5.3. The results achieved by the undamped defection correction method are compared with those that used damping coefficients 0.6 and 1.1 at the sensitive and nonsensitive cells, respectively, and with the converged solution.

Pressure distributions are given at the midsection of the outer wing after 10 and 15 defect-correction iterations which are described by Figs. 6 and 8, respectively. A closeup of the difficult-to-converge region in Figs. 6 and 8 is given in Figs. 7 and 9.

We observe that the use of variable damping coefficients significantly improves the rate of convergence. In particular, it quickly reduces the amplitudes of oscillations at the foot of the shock. In this location the shock boundary-layer interaction produces a region of reverse flow. The shock pattern is clearly seen in Fig. 10, which represents the upper surface pressure distribution. Figure 11 displays the streamwise velocity component just above the wing. The most inner "island" (or contour) represents a region of reverse flow.

6. CONCLUSIONS

A multigrid solver has been developed and applied to a 3D model of turbulent compressible transonic flow at a high Reynolds number. A finite-volume discretization is employed, with essentially non-oscillatory (ENO) discretization of the convection terms. The solver extends the capabilities of its predecessors by the introduction of the complete nonlinear (FAS) multigrid framework, implemented with a defect-correction technique, and by the allowance of local grid refinement where required.

These features were tested on the ONERA M-6 wing. The results with and without a locally refined grid were compared to wind-tunnel experiments. They exhibit a good agreement. The locally refined grid provided accuracy comparable to that of a full additional fine grid and at a much smaller computational cost. This efficient utilization of the locally refined grid was made possible by the multigrid structure, which allows the solution in the refined region to influence the flow in the unrefined regions (and vice versa). We expect this effect to become more important as more levels of local refinement are employed. An additional check of robustness and accuracy of the proposed method was performed by solving the inviscid flow over the ONERA M-6 wing on a set of grids previously used for the Navier–Stokes computations. The lack of natural dissipation in combination with high aspect ratio of cells, which is typical of the stretched "Navier–Stokes grids," makes this test highly demanding. The comparison with the theoretical data shows that the present method successfully resolves the convection terms of the Navier–Stokes equations without requiring artificial dissipation. Improvements in code performance were successfully tested on an example of a cranked and twisted transonic wing with highly cusped profiles. The defect-correction driven multigrid approach exhibited a robust behavior in this case which is a representative of complicated flow-fields containing significant regions of separated flow. The overall acceleration, which is due to the combination of the present nonlinear multigrid framework and the use of local refinements, is estimated to be about an order of magnitude in the case of complicated wing geometries.

In the future, we plan to implement this solver in a multiblock framework, which eventually will allow us to model flow over far more complicated geometries. This code will be

implemented in parallel, based on our parallel implementation of its predecessor, which is presently being developed.

REFERENCES

1. S. Reddy and M. Papadakis, *Artificial Viscosity Models for the Navier–Stokes Equations and Their Effect on Drag Prediction*, presented at the AIAA 31st Aerospace Sciences Meeting, January 1993, Reno, Nevada, Meeting Paper 93-0193 (AIAA Press, Washington, DC, 1993).
2. R. Varma and D. A. Cauphey, *Evaluation of Navier–Stokes Solutions Using the Integrated Effect of Numerical Dissipation*, presented at the AIAA 31st Aerospace Sciences Meeting, January 1993, Reno, Nevada, Meeting Paper 93-0539 (AIAA Press, Washington, DC, 1993).
3. A. Harten, B. Engquist, S. Osher, and S. Chakravarthy, Uniformly high order accurate non-oscillatory schemes, I, *J. Comput. Phys.* **71**, 231 (1987).
4. C.-W. Shu and S. Osher, Efficient implementation of essentially non-oscillatory shock-capturing schemes, *J. Comput. Phys.* **83**, 32 (1989).
5. B. Epstein and A. Nachshon, *An ENO Navier–Stokes Solver Applied to 2-D Subsonic, Transonic and Hypersonic Aerodynamic Flows*, presented at the AIAA 32nd Aerospace Sciences Meeting, January 1994, Reno, Nevada, Meeting Paper 94-0303 (AIAA Press, Washington, DC, 1994).
6. B. Epstein, A. Jacobs, and A. Nachshon, Aerodynamically accurate three-dimensional Navier–Stokes method, *AIAA J.* **35**(6), 1089 (1997).
7. B. Epstein, A. Jacobs, and A. Nachshon, *An ENO 3-D Multilevel Navier–Stokes Method: Towards an Aerodynamically Accurate CFD Tool*, presented at the 15th International Conference on Numerical Methods in Fluid Mechanics, Monterey, California, June 1996.
8. G. Jiang and C.-W. Shu, Efficient implementation of weighted ENO schemes, *J. Comput. Phys.* **126**, 202 (1996).
9. C.-W. Shu, *Essentially Non-Oscillatory and Weighted Essentially Non-Oscillatory Schemes for Hyperbolic Conservation Laws*, ICASE Report 97-65 (November 1997).
10. A. Brandt, Multi-level adaptive computations in fluid dynamics, *AIAA J.* **18**(10), 100 (1980).
11. A. Brandt and I. Yavneh, On multigrid solution of high-reynolds incompressible entering flows, *J. Comput. Phys.* **101**, 151 (1992).
12. I. Yavneh, Coarse-grid correction for nonelliptic and singular perturbation problems, *SIAM J. Sci. Comput.* **19**(5), 1682 (1998).
13. B. Epstein, A. Luntz, and A. Nachshon, Cartesian euler method for arbitrary aircraft configurations, *AIAA J.* **30**(3), 679 (1992).
14. A. Jameson, Schmidt, and E. Turkel, *Numerical Solution of the Euler Equations by Finite Volume Methods Using Runge–Kutta Time-Stepping Schemes*, presented at the AIAA 14th Fluid and Plasma Mechanics Conference, Palo-Alto, CA, Meeting Paper 81-1259 (AIAA Press, Washington, DC, 1981).
15. D. J. Mavriplis, Three-dimensional multigrid reynolds-averaged Navier–Stokes solver for unstructured meshes, *AIAA J.* **33**(3), 445 (1995).
16. D. J. Mavriplis, Directional agglomeration multigrid techniques for high-reynolds-number viscous flows, *AIAA J.* **37**(10), 1222 (1999).
17. M. Griebel, T. Neunhoeffer, and H. Regler, Algebraic multigrid methods for the solution of the Navier–Stokes equations in complicated geometries, *Int. J. Numer. Meth. Fluids.* **26**(3), 281 (1998).
18. F.-P. Lin, Multigrid solutions of the Euler and Navier–Stokes equations on unstructured grids, *Int. J. Numer. Meth. Fluids* **29**(8), 921 (1999).
19. A. Brandt, *1984 Multigrid Guide with Applications to Fluid Dynamics*, Monograph, GMD-Studie 85 (GMD-FIT, Postfach 1240, D-5205, St. Augustin 1, West Germany, 1985).
20. J.-A. Desideri and P. W., Convergence analysis of the defect correction iteration for hyperbolic problems, *SIAM J. Sci. Comput.* **16**(1), 88 (1995).
21. B. Koren, Multigrid and defect correction for the steady Navier–Stokes equations, *J. Comput. Phys.* **87**, 25 (1990).

22. W. A. Mulder, A high-resolution Euler solver based on multigrid, semi-coarsening, and defect correction, *J. Comput. Phys.* **100**, 91 (1992).
23. E. Dick, Second-order formulation of multigrid method for steady Euler equations through defect correction, *J. Comput. Appl. Math.* **35**(1), 159 (1991).
24. A. Brandt and V. Mikulinsky, On recombining iterants in multigrid algorithms and problems with small islands, *SIAM J. Sci. Comput.* **16**(1), 20 (1995).
25. B. S. Baldwin and H. Lomax, *Thin layer Approximation and Algebraic Model for Separated Turblent flows*, Technical Paper 78-257 (AIAA Press, Washington, DC, 1978).